

The GAPS Programme with HARPS-N at TNG

VII. Putting exoplanets in the stellar context: magnetic activity and asteroseismology of τ Bootis A[★]★★

F. Borsa¹, G. Scandariato², M. Rainer¹, A. Bignamini³, A. Maggio⁴, E. Poretti¹, A. F. Lanza², M. P. Di Mauro⁵, S. Benatti⁶, K. Biazzo², A. S. Bonomo⁷, M. Damasso⁷, M. Esposito^{8,9}, R. Gratton⁶, L. Affer⁴, M. Barbieri¹⁰, C. Boccato⁶, R. U. Claudi⁶, R. Cosentino^{2,11}, E. Covino¹², S. Desidera⁶, A. F. M. Fiorenzano¹¹, D. Gandolfi^{2,13}, A. Harutyunyan¹¹, J. Maldonado⁴, G. Micela⁴, P. Molaro³, E. Molinari^{11,14}, I. Pagano², I. Pillitteri^{4,15}, G. Piotto^{6,16}, E. Shkolnik¹⁷, R. Silvotti⁷, R. Smareglia³, J. Southworth¹⁸, A. Sozzetti⁷, B. Stelzer⁴

¹ INAF – Osservatorio Astronomico di Brera, Via E. Bianchi 46, 23807 Merate (LC), Italy

² INAF – Osservatorio Astrofisico di Catania, Via S. Sofia 78, 95123, Catania, Italy

³ INAF – Osservatorio Astronomico di Trieste, via Tiepolo 11, 34143 Trieste, Italy

⁴ INAF – Osservatorio Astronomico di Palermo, Piazza del Parlamento, 1, 90134, Palermo, Italy

⁵ INAF-IAPS Istituto di Astrofisica e Planetologia Spaziali, Via del Fosso del Cavaliere 100, 00133, Roma, Italy

⁶ INAF – Osservatorio Astronomico di Padova, Vicolo dell’Osservatorio 5, 35122, Padova, Italy

⁷ INAF – Osservatorio Astrofisico di Torino, Via Osservatorio 20, 10025, Pino Torinese, Italy

⁸ Instituto de Astrofísica de Canarias, C/Via Láctea S/N, 38200 La Laguna, Tenerife, Spain

⁹ Departamento de Astrofísica, Universidad de La Laguna, 38205 La Laguna, Tenerife, Spain

¹⁰ Department of Physics, University of Atacama, Copayapu 485, Copiapo, Chile

¹¹ Fundación Galileo Galilei - INAF, Rambla José Ana Fernández Pérez 7, 38712 Breña Baja, TF - Spain

¹² INAF – Osservatorio Astronomico di Capodimonte, Salita Moiarillo 16, 80131, Napoli, Italy

¹³ Landessternwarte Königstuhl, Zentrum für Astronomie der Universität Heidelberg, Königstuhl 12, 69117 Heidelberg, Germany

¹⁴ INAF - IASF Milano, via Bassini 15, 20133 Milano, Italy

¹⁵ Harvard-Smithsonian Center for Astrophysics, 60 Garden Street, Cambridge, MA, 02138, USA

¹⁶ Dip. di Fisica e Astronomia Galileo Galilei – Università di Padova, Vicolo dell’Osservatorio 2, 35122, Padova, Italy

¹⁷ Lowell Observatory, 1400 W. Mars Hill Road, Flagstaff, AZ, 86001, USA

¹⁸ Astrophysics Group, Keele University, Staffordshire, ST5 5BG, UK

Received ; accepted

Abstract

Aims. We observed the τ Boo system with the HARPS-N spectrograph to test a new observational strategy aimed at jointly studying asteroseismology, the planetary orbit, and star-planet magnetic interaction.

Methods. We collected high-cadence observations on 11 nearly consecutive nights and for each night averaged the raw FITS files using a dedicated software. In this way we obtained spectra with a high signal-to-noise ratio, used to study the variation of the Ca II H&K lines and to have radial velocity values free from stellar oscillations, without losing the oscillations information. We developed a dedicated software to build a new custom mask that we used to refine the radial velocity determination with the HARPS-N pipeline and perform the spectroscopic analysis.

Results. We updated the planetary ephemeris and showed the acceleration caused by the stellar binary companion. Our results on the stellar activity variation suggest the presence of a high-latitude plage during the time span of our observations. The correlation between the chromospheric activity and the planetary orbital phase remains unclear. Solar-like oscillations are detected in the radial velocity time series: we estimated asteroseismic quantities and found that they agree well with theoretical predictions. Our stellar model yields an age of 0.9 ± 0.5 Gyr for τ Boo and further constrains the value of the stellar mass to $1.38 \pm 0.05 M_{\odot}$.

Key words. Stars: individual: τ Boo – planetary systems – Asteroseismology – techniques: spectroscopic – Stars: activity

1. Introduction

While the number of confirmed exoplanets is rapidly increasing, we are improving our ability to characterize them by studying their parent stars and the star-planet tidal or magnetic interactions. At the moment, the most interesting targets for characterization are transiting exoplanets, but the large population of non-transiting planets solicits new methods and observation strategies for this purpose.

With the intent of characterizing planetary systems with a spectro-photometric approach, we selected the well-known

Send offprint requests to: F. Borsa
e-mail: francesco.borsa@brera.inaf.it

* Based on observations made with the Italian Telescopio Nazionale Galileo (TNG) operated on the island of La Palma by the Fundación Galileo Galilei of the INAF at the Spanish Observatorio Roque de los Muchachos of the IAC in the frame of the program Global Architecture of the Planetary Systems (GAPS).

** Table 1 is only available in electronic form at the CDS via anonymous ftp to cdsarc.u-strasbg.fr (130.79.128.5) or via http://cdsweb.u-strasbg.fr/cgi-bin/qcat?J/A+A/

system τ Bootis A (HD 120136, F6V, $V=4.49$) as a test case in the Global Architecture of Planetary Systems¹ (GAPS, Covino et al. 2013) programme. GAPS is a joint effort of Italian researchers in collaboration with a few experts abroad, and the GAPS team manages a long-term observational program with the high-precision HARPS-N spectrograph² (Cosentino et al. 2012) at the Telescopio Nazionale Galileo (TNG). τ Boo A is included in the subprogram dedicated to the characterization of planetary systems through studies of the interactions between the planets and their central stars. τ Boo's brightness allows for high-resolution spectroscopy and asteroseismology with a limited investment of telescope time.

The bright F6V star has a faint M2V companion (τ Boo B, separation 1.83", Drummond 2014), forming a long-period binary system. The primary component (hereafter τ Boo for the sake of uniformity with current literature) was first claimed to host a planet with a period of 3.312 days by Butler et al. (1997); they used the radial velocity (RV) method. Thanks to its brightness, this system was employed in the past to develop new analysis techniques that have later been applied to other stars. Among the most important discoveries are the definition of upper limits on reflected starlight, which provides a maximum value for the planet's albedo (Collier Cameron et al. 1999; Rodler et al. 2010), the spectroscopic detection of CO absorption lines in the planet atmosphere, which permitted determining the inclination angle of the system and thus the exact mass of the planet ($M_p=5.95 \pm 0.28 M_{Jup}$, Brogi et al. 2012; Rodler et al. 2012) and, very recently, the first detection of water vapor in the atmosphere of a non-transiting exoplanet (Lockwood et al. 2014).

τ Boo was also considered in searches for effects of star-planet magnetic interaction (SPMI). A peculiar characteristic of this star is the optically variable modulation of the light curve that is probably due to photospheric spots that persisted at fixed longitudes for a few hundred days, as observed by the MOST satellite (Walker et al. 2008). SPMI is a long-debated issue, with the best evidence coming from a modulation of chromospheric activity tracers phased with the planetary orbital period rather than with the stellar rotation period (Shkolnik et al. 2005, 2008; Lanza 2009, 2012).

Assessment of this behavior requires long-term monitoring of stars with close-in massive planets (hot Jupiters), very high signal-to-noise spectra ($S/N > 300$ at 3950Å), and adequate resolving power ($R \geq 80000$) to measure variability in the core of deep chromospheric lines such as the Ca II H&K doublet. Detecting periodicities equal to the planetary period is crucial because variability can be due to intrinsic stellar activity, not related to the presence of hot Jupiters. On the other hand, the study of stellar activity is important as a source of noise in the search and characterization of new planets in extra-solar systems.

In the case of τ Boo, previous searches for SPMI in the Ca II H&K lines were ambiguous (Shkolnik et al. 2005). One possible reason is that SPMI is due to magnetic stresses between the stellar and planetary magnetic fields, but this effect is very limited in τ Boo because the stellar rotation is known to be synchronized with the orbital motion of the planet (e.g., Henry et al. 2000). Nonetheless, this system remains an interesting target because the parent star shows evidence of magnetic cycles, with yearly polarity reversals (e.g., Catala et al. 2007; Donati et al. 2008; Fares et al. 2009).

Asteroseismology of stars hosting exoplanets received a great boost from the photometric time series collected by space missions. On the other hand, spectroscopic campaigns aimed at detecting solar-like oscillations are very hard to organize because a long time baseline is required to resolve and identify the excited modes. For instance, Bazot et al. (2012) were able to obtain a measure of the large separation of 18 Sco by means of 2833 data points collected over 12 complete nights. It is difficult to insert an asteroseismic program in a large project such as GAPS, which covers a multiplicity of subprograms and goals with limited telescope time. Moreover, the exposure times have to be very short to monitor the solar-like oscillations, and consequently, the asteroseismic targets have to be bright stars. Therefore we used the scientific case of τ Boo as a pathfinder, applying the high-cadence observational strategy for asteroseismic purposes and matching it with some exoplanetary goals (search for additional planets and study of the star-planet interaction). The paper is structured as follows: Sect. 2 presents the observations and describes the data reduction. Section 3 is devoted to the spectral analysis, with results presented in Sect. 4 (stellar parameters), Sect. 5 (orbital parameters), Sect. 6 (stellar activity), Sect. 7 (asteroseismology), and Sect. 8 (evolutionary stage). Conclusions are presented in Sect. 9.

2. Observations and data reduction

τ Boo was observed with HARPS-N on 11 nights between April 13 and May 8, 2013. Very good phase coverage of the orbital period of the planet was obtained. A few more observations were made in April and July 2014 to characterize the observed long-term trend. Simultaneous Th-Ar calibration was used to achieve high RV precision. The complete set of observations is shown in Table 1. When possible, we observed the fast-rotating, hot star η UMa (B3V, $V=1.84$, $V \sin i = 205 \text{ km s}^{-1}$) immediately afterwards; this was our tool to remove telluric lines.

Table 1. HARPS-N RV observations of τ Boo. This table is available in its entirety online at the CDS.

BJD _{UTC} -2450000.	RV (m s ⁻¹)	RV err (m s ⁻¹)	Bis. span (m s ⁻¹)
6396.517465	-16145.21	0.83	-104.71
6396.518460	-16136.13	0.83	-114.74
6396.519444	-16141.63	0.84	-109.08
6396.520439	-16141.12	0.80	-102.26
...

To study the star-planet interaction, we needed to reach a high signal-to-noise ratio (S/N) near the Ca II H&K lines. To match this requirement with a single exposure would cause the saturation of the rest of the spectrum, given the spectral energy distribution of τ Boo and the lower efficiency of HARPS-N in the blue region. The need to avoid saturation was combined with the requirements of an asteroseismic feasibility study of τ Boo with HARPS-N, allowing us to make a synergy between different science themes of the GAPS campaign. Our observational strategy consisted of taking several one-minute exposures and then averaging them to obtain a single spectrum with a very high S/N . In this way, we obtained both the high-cadence spectra to monitor the solar-like oscillations and the mean high S/N spectra to study the Ca II H&K variations over the orbital period of

¹ http://www.oact.inaf.it/exoit/EXO-IT/Projects/Entries/2011/12/27_GAPS.html

² <http://www.tng.iac.es/instruments/harps/>

the planet. Moreover, we also obtained RV values to study the long-term variability of the system.

We developed an interactive program written in Python (Borsa et al. 2013) to average the raw images pixel by pixel, adjusting the header of the created files. The resulting mean FITS files are ready to be passed through the HARPS-N pipeline. In this way they are reduced exactly in the same way as all the FITS files acquired with HARPS-N (Table 2).

The Julian dates of the mean files calculated by the pipeline are not the correct dates because of the overhead time between the single exposures. This time is ~ 25 sec, therefore its influence on consecutive 1 min exposures is relevant. We corrected for this by taking an average of the Julian dates of the single images, weighted on their respective S/N: in this way, we introduced a sort of exposure-meter information in the mean file. The RVs were then corrected for the change in the barycentric Earth radial velocity (BERV) between the pipeline-estimated Julian date and the corrected date. For this purpose, we created a new tool and verified it to be comparable with the HARPS-N pipeline at the level of $\sim 3 \text{ cm s}^{-1}$ (Borsa et al. 2013).

Table 2. RVs for the τ Boo nightly mean spectra. ϕ refers to the orbital phase of the planetary companion, based on the ephemeris of Sect. 5 and considering the planetary inferior conjunction as $\phi=0$.

Night	BJD _{UTC} -2450000	RV [m s^{-1}]	RV err [m s^{-1}]	ϕ
1	6396.531788	-16135.08	0.86	0.73
2	6397.536059	-16716.81	0.77	0.03
3	6398.499820	-17016.77	0.93	0.33
4	6399.548081	-16231.25	1.39	0.65
5	6401.498724	-17085.13	0.79	0.23
6	6402.497328	-16501.11	1.31	0.53
7	6406.653040	-16169.98	0.78	0.79
8	6407.703825	-16904.41	0.89	0.10
9	6408.686713	-16878.51	0.96	0.40
10	6410.680969	-16603.65	1.34	0.00
11	6421.517542	-17054.54	0.97	0.27

The data (324 single exposures and 11 mean exposures) were finally reduced using the HARPS-N data reduction software (DRS) pipeline on the Yabi platform. Yabi (Hunter et al. 2012) is a Python web application installed at IA2³ in Trieste that allows authorized users to run the HARPS-N DRS pipeline on their own proprietary data with custom input parameters.

The pipeline installed at the TNG estimates the radial velocities of the targets by computing a cross-correlation function (CCF, Pepe et al. 2002) using the best-suited line mask of the available masks (G2, K5, or M2 spectral type). Taking advantage of the Yabi platform, we were able to create and implement a new custom mask for τ Boo (Rainer 2013; Gratton 2013). Using the standard G2 mask as a starting point, we measured the depths of several unblended lines in a well-exposed, high S/N τ Boo spectrum. From these measurements we found the following empirical correlation between the line depths (LD) of the G2 mask and those of the τ Boo spectrum: $LD_{\tau \text{ Boo}} = 0.0409321 \cdot e^{2.80654 \cdot LD_{G2}}$. Using this equation, we corrected the values of the line depths in the standard G2 mask and created the new custom mask (3625 photospheric lines) that we used for the data reduction. In addition to this, we increased the width of

the half-window of the weighted CCF from the default value of 20 up to 30 km s^{-1} (about twice the value of $V \sin i$ of the star) to clearly cover the continuum around the wings of the mean line profile. These improvements reduced the RV errors by $\sim 5\%$.

3. Spectral analysis

The analysis of the magnetic activity of τ Boo was performed using the nightly high S/N mean spectra. The CCF provided by the DRS pipeline was computed by cross-correlating the spectrum of τ Boo with the custom mask (see Sect. 2): it is thus essentially a high S/N mean line profile, and it is highly sensitive to the presence of active regions on the stellar photosphere.

To study the variability of the photospheric activity, we monitored the line profile variations of the CCF, in particular its contrast (CCFc) and full-width at half-maximum (FWHM), the bisector inverse slope (BIS, Gray 2008), and the v_{asy} parameter (Figueira et al. 2013). We computed these indicators by means of custom-made routines, developed by our team for HARPS-N spectra.

We also monitored the variability of the chromospheric activity. We focused on the Ca II H&K lines (3968.47 Å and 3933.66 Å), the Na I D₁₂ doublet (5889.95 Å and 5895.92 Å), the He I D₃ triplet (blend at 5875.62 Å), and the H α line (6562.79 Å) as chromospheric diagnostics.

The chromospheric indicators were analyzed starting from the HARPS-N one-dimensional spectra reduced with the DRS pipeline, which computes the localization of spectral orders on the two-dimensional images, performs order extraction and stitching, corrects for flat-fielding, rejects cosmic-rays, and calibrates the wavelength. Our analysis is based on the differential comparison between the spectra in the series realigned in the wavelength space. This approach allows us to avoid the uncertainties related to the absolute flux calibration and continuum normalization and is therefore more robust than the method adopted by Scandariato et al. (2013), which depends on the normalization to the continuum (a difficult task in the presence of broad lines such as the Ca II H&K and order stitching).

Here we discuss how we reduced the data to perform the differential analysis, while in Sect. 6.1 we analyze the variability in the spectra of τ Boo. In the following analysis we excluded the data point of night 4 because it has low S/N, and no spectroscopic standard star was observed because of bad weather.

The Na I D₁₂ doublet, the He I D₃ triplet, and the H α line are affected by telluric contamination, which is variable from night to night as a result of different airmasses and sky conditions. For each night of observation, telluric features were removed from the target spectrum by comparing it with the spectrum of the standard star η UMa. We corrected for telluric absorption using the task `telluric` in IRAF (Tody 1993). In contrast, the Ca II H&K spectral region of the standard star does not show any telluric feature above noise. Telluric correction was therefore not performed on the corresponding spectral interval of τ Boo to preserve the original S/N.

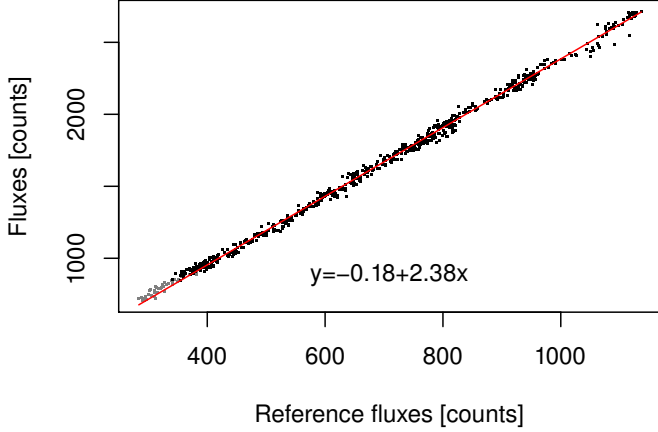
To carry out the spectral differential analysis, we needed to rescale all the spectra to the same flux scale. To this purpose, we selected the spectrum at mid-time (i.e., the spectrum of night 6) with respect to which we performed the differential spectral analysis. This choice aims at minimizing any time-dependent instrumental effect along the time series of spectra (see below).

For each diagnostic we extracted the corresponding spectral region, and we compared each spectrum in the series with the reference spectrum on a pixel-by-pixel basis (Fig. 1), taking advantage of the wavelength stability of HARPS-N. In this way,

³ <http://ia2.oats.inaf.it/>

Table 3. Spectral ranges used for the analyzed chromospheric diagnostics.

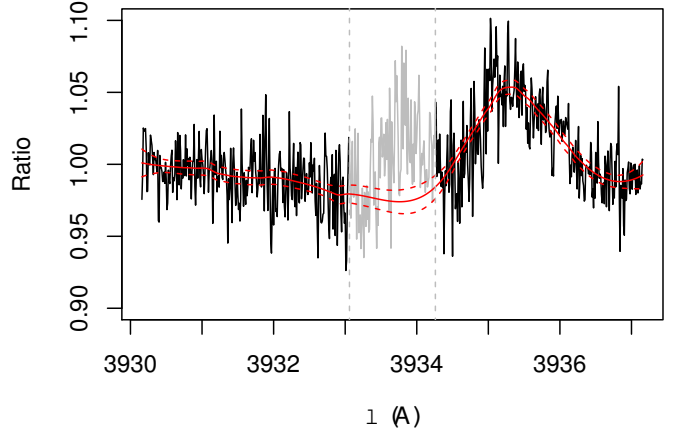
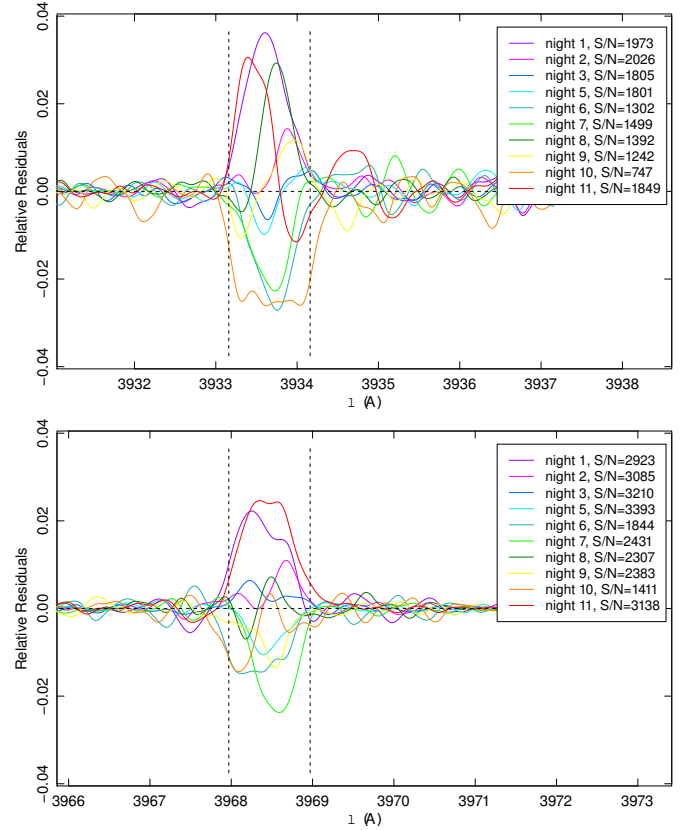
Line	Vacuum wavelength (Å)	Spectral width (Å)	Core width (Å)
Ca II K	3933.66	3.5	0.5
Ca II H	3968.47	3.5	0.5
Na I D ₂	5889.95	3.5	0.3
Na I D ₁	5895.92	3.5	0.3
He I D ₃	5875.72	3.5	0.6
H α	6562.79	3.5	0.5

**Figure 1.** Example of the flux calibration of the mean spectrum of night 3 over the mean spectrum of night 6 in the Ca II K spectral range. The best fit (red line) is computed using the black dots, which represent instrumental fluxes out of the line core. The instrumental fluxes of the line core (in gray) are not included in the fit. The equation of the best fit is also shown.

the reference spectrum defined the common flux scale, and all the other spectra were rescaled accordingly using a linear best fit of the flux vs flux relation. The intercept adjusts the background level, while the slope rescales intrinsic stellar fluxes. Line cores were excluded from the best fit to avoid any intrinsic nonlinearity that might have been introduced by chromospheric variability. The widths of the analyzed spectral ranges and the line cores are reported in Table 3.

This procedure generally led to satisfactory results, that is, fluxes were well aligned along a straight line (Fig. 1). Still, in a few cases especially in the Ca II K line, the residuals of the fit were higher by $\sim 5\%$ than the noise over small wavelength ranges, typically $\lesssim 1$ Å (Fig. 2). These distortions, frequently observed during the first year of operation of HARPS-N, are not relevant in the measurement of RVs, but introduce spectral inhomogeneities on a night-to-night basis that may hamper the SPMI analysis. To correct for them, we divided the spectra pixel by pixel by the reference spectrum, and we locally fitted the ratio with a low-order polynomial, excluding a narrow window centered on the line cores where the SPMI signal might be mistaken as an instrumental effect. Finally, each spectrum was divided by the fitted ratio to remove the low-order flux variations. In Fig. 2 we show an example of the low-order correction in the Ca II K line.

After removing the distortions, we averaged the time series of the corrected mean spectra for each spectral range. Then we computed the relative residuals for each mean spectrum with re-

**Figure 2.** Example of the low-order correction of the Ca II K line. The black line is the ratio of one spectrum in the series to the reference spectrum, while the red line is the low-order fit (95% confidence band is shown with red dashes). The vertical dashed lines bracket the line core, in gray, which is excluded from the fit.**Figure 3.** Residuals relative to the average spectrum of the Ca II K (top panel) and H (bottom panel) lines. The color code (online version only) is reported in the legend, together with the S/N in the line for a 1 Å spectral element (night 4 has been excluded, see text). The residuals have been smoothed to avoid cluttering; for this reason, they slightly exceed the vertical dashed lines.

spect to the averaged spectrum and integrated them over a ~ 1 Å window around the line center to obtain the integrated relative deviation (IRD). Figure 3 shows the residuals, which have been smoothed to show the variability in the Ca II H&K line core more clearly. We computed the uncertainties on the IRDs by summing

in quadrature the photon noise and the uncertainties on flux calibration and low-order correction. In this way, we take into account the same sources of error more than once, thus obtaining an upper limit to the true uncertainty.

We note that the relative residuals in the line cores are comparable to or slightly smaller than our low-order corrections to the spectra. The reliability of our approach rests on the verification that the recovered Ca II H&K signals (IRDs) are reasonably correlated, and the same holds for Ca II H+K vs H_α IRDs (Sect. 6.1). We have verified that our low-order correction improves these physically meaningful correlations.

4. Stellar parameters

We derived the physical parameters of τ Boo by means of fitting synthetic spectra (ATLAS9 stellar atmosphere models, Castelli & Kurucz 2004) to a normalized HARPS-N mean file using the SME software by Valenti & Piskunov (1996). The hydrogen lines could not be used to determine the temperature because they span several spectral orders, which introduces problems in the normalization of the spectra. Therefore we used the region between 5160 and 5190 Å, where the Mg triplet is found.

We computed the $V \sin i$ using the Fourier transform of the CCF of a mean spectrum (see Sect. 4.1). This value was kept fixed in the fit while the other parameters were left free to vary. Table 4 shows our results, which agree well with the values found in the literature (e.g., Santos et al. 2013). A portion of the observed and synthetic spectra is shown in Fig. 4. An independent check of the stellar parameters was made with the method based on the equivalent widths of spectral absorption lines (Sousa et al. 2007; Biazzo et al. 2012, and references therein). Even if this method is not preferable because of the high $V \sin i$ value of τ Boo, results were compatible with those estimated with the synthetic spectra method.

Table 4. Stellar parameters derived for τ Boo.

Parameter	Value
T_{eff} [K]	6399 ± 45
$\log g$ [cm s ⁻¹]	4.27 ± 0.06
[Fe/H]	0.26 ± 0.03
$V \sin i$ [km s ⁻¹]	14.27 ± 0.06
Luminosity [L_\odot]	3.06 ± 0.16
Mass [M_\odot]	1.39 ± 0.25
Radius [R_\odot]	1.42 ± 0.08
V_{breakup} [km s ⁻¹]	352 ± 67

We determined stellar radius and mass (Table 4) by combining the spectroscopic results with the parallax (64.03 ± 0.19 mas, van Leeuwen 2007) and using a bolometric correction (-0.0078 , Torres 2010; Flower 1996).

4.1. Differential rotation

We found evidence of solar-like differential rotation in τ Boo from studying the Fourier transform of the mean line profiles of the HARPS-N mean spectra. We used two different mean line profiles: the CCF computed by the HARPS-N pipeline and the profile obtained using the LSD software (Donati et al. 1997) on the wavelength regions 4415-4805, 4915-5285, and 5365-6505 Å. The CCF was computed using the Yabi interface, which

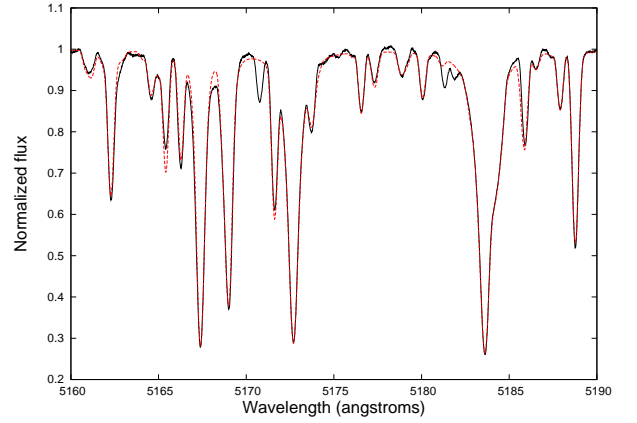


Figure 4. Fit of the observed mean spectrum (solid black line) with the synthetic spectrum (dashed red line) in the wavelength region considered, using the SME software.

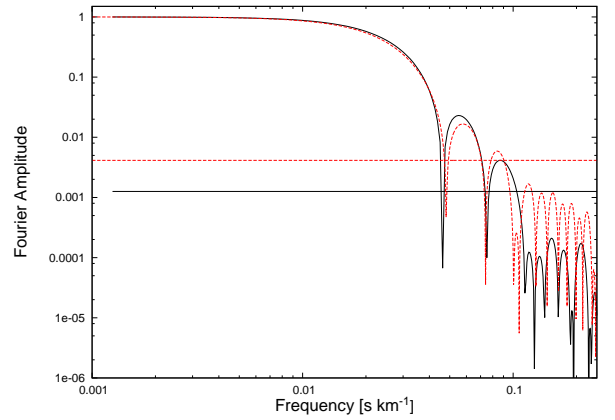


Figure 5. Amplitude of the Fourier transform of a mean line profile. Red dashed line refers to the LSD software, black solid line to the HARPS-N CCF. The horizontal lines show the noise level.

means that we were able to reduce the spectra with our custom mask, and we further increased the CCF half-window width up to 40 km s⁻¹, to ensure that we captured the whole mean line profile and the continuum.

We used a Fourier transform on both the LSD and the CCF profiles (Fig. 5) and found the values of the first two zero positions q_1 and q_2 . The q_1 position gives an estimate of the projected rotational velocity $V \sin i$, while the ratio q_2/q_1 is an indicator of differential rotation (Reiners & Schmitt 2002), either solar-like ($q_2/q_1 < 1.72$) or antisolar ($q_2/q_1 > 1.83$). We found $q_2/q_1 = 1.53 \pm 0.08$ for the LSD profile and $q_2/q_1 = 1.63 \pm 0.04$ for the CCF. The larger error in the LSD profile arises probably from the fact that we did not use the whole spectral range. These values are compatible with the results from Reiners (2006) ($q_2/q_1 = 1.57 \pm 0.04$) and Catala et al. (2007) ($q_2/q_1 = 1.60 \pm 0.02$).

The q_2/q_1 we found can indicate either solar-like differential rotation (equator rotating faster than the poles) or strong gravity-darkening in a rigidly rotating star. In the second case, the following empirical equation (Reiners 2003) can be used to infer the rotational velocity of the star:

$$q_2/q_1 = 1.75 + av + bv^2, \quad (1)$$

where a and b are parameters that depend on the stellar spectral type. In particular, these parameters are $a = 0.172 \times 10^{-3}$ and $b = -0.993 \times 10^{-6}$ for F0 stars and $a = 0.184 \times 10^{-3}$ and $b = -0.116 \times 10^{-5}$ for G0 stars. τ Boo is classified as an F6 star, falling in the middle of these values, which means that to justify the values of q_2/q_1 found by means of rigid rotation, the star's rotational velocity should be either between 415 and 450 km s^{-1} (in the CCF case) or between 520 and 550 km s^{-1} (in the LSD case). Considering the values of mass and radius of Table 4, we can compute the breakup velocity $v_{\text{breakup}} = 352 \text{ km s}^{-1}$.

For the values q_2/q_1 to be caused by gravity-darkening, the star would have to rotate faster than the breakup velocity. We can therefore reliably establish that the two q_2/q_1 values found show solar-like differential rotation in τ Boo.

Adopting an inclination angle for the star $i = 40^\circ$ (Donati et al. 2008) and using the q_2/q_1 values, we computed the differential rotation parameter $\alpha = \frac{\Delta\Omega}{\Omega_0}$, where Ω_0 is the equatorial angular velocity of the star and $\Delta\Omega$ is the difference between the equatorial and polar angular velocities. Using the empirical relation (Reiners & Schmitt 2003)

$$\frac{\alpha}{\sqrt{\sin i}} = 2.74 - 5.16 \left(\frac{q_2}{q_1} \right) + 4.32 \left(\frac{q_2}{q_1} \right)^2 - 1.30 \left(\frac{q_2}{q_1} \right)^3, \quad (2)$$

we found $\alpha = 0.24 \pm 0.07$ from $q_2/q_1 = 1.53$ (LSD profile) and $\alpha = 0.16 \pm 0.04$ from $q_2/q_1 = 1.63$ (CCF), both compatible with the value $\alpha = 0.18$ found by Catala et al. (2007). The LSD result is exactly the same as the differential rotation found by Donati et al. (2008) using spectropolarimetric measures.

Our work shows that the LSD profile and the CCF provide similar values of q_2/q_1 . As such, the CCF computed internally by the HARPS-N pipeline can be used as an indicator of differential rotation, at least for high S/N spectra.

5. Orbital fit

We used data from Table 1 to perform the orbital fit, but when multiple exposures were taken during one night, we used the RV value corresponding to the nightly mean spectra (e.g., Table 2) to be independent of stellar oscillations. The final HARPS-N set of measurements is composed of 20 RV points. In addition to our HARPS-N data, we used the recently released archival data of the Lick Observatory (Fischer et al. 2014). These data were obtained with four different iodine-cell setups (identified as number 2, 13, 6, and 8 in Table 5) that were taken in consideration during the analysis adding a RV shift as a free parameter to each set. We excluded all the data with $\sigma > 30 \text{ m s}^{-1}$ (e.g., all the data of Lick setup number 2) and those that did not maintain the same instrumental setup continuously. We used 166 Lick RV measurements in the orbital fit. By combining Lick and HARPS-N data, we obtained a dataset composed of 186 measurements, spanning a time interval of about 20 years.

We fitted the RVs with a Levenberg-Marquardt algorithm (Wright & Howard 2009), using a two-planet model (Fig. 6) to take into account both the short-term variability due to the known planet and the long-term trend due to the stellar binary companion (Sect. 5.1). To estimate the error-bars, we used a bootstrapping code (Wang et al. 2012). The orbital parameters obtained are reported in Table 5.

We analyzed the RV residuals shown in the bottom panel of Fig. 6 in frequency, but did not find any trace of additional periodicity. We note in particular that RV residuals of HARPS-N show a clear correlation with the pipeline-estimated bisector

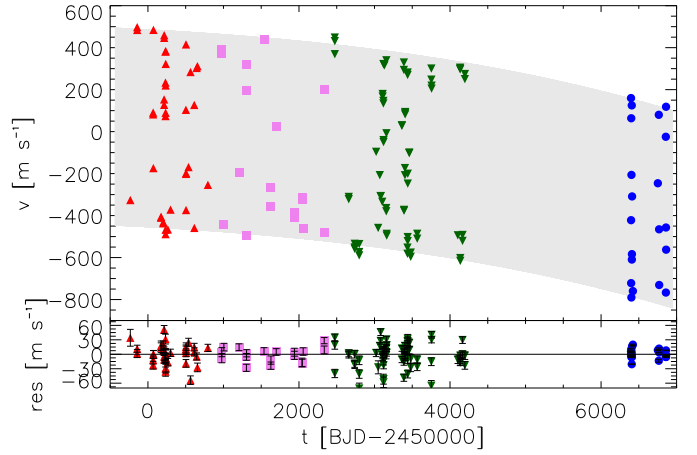


Figure 6. Two-objects orbital fit (gray) for the Lick Observatory archival data (red upward triangles, pink squares, and green downward triangles corresponding to the different setup configurations 13, 6, and 8 respectively) and HARPS-N data (blue circles). RV residuals are shown in the bottom plot.

Table 5. Orbital parameters estimated for the τ Boo system. Period and periastron of the binary companion τ Boo B were fixed to those of the astrometric solution reported by Drummond (2014).

Parameter	Value
τ Boo b	
Period [days]	$3.3124568 \pm 6.9 \times 10^{-6}$
$T_{\text{periastron}}$ [BJD _{UTC} -2450000]	6400.94 ± 0.30
K [m s^{-1}]	471.73 ± 2.97
e	0.011 ± 0.006
ω [deg]	113.4 ± 32.2
γ [m s^{-1}]	0.0
$m \sin i$ [M_{Jup}]	4.32 ± 0.04
semi-major axis [AU]	0.049 ± 0.003
τ Boo B	
Period [years]	964 (<i>fixed</i>)
$T_{\text{periastron}}$ [BJD _{UTC} -2450000]	12670 (<i>fixed</i>)
K [m s^{-1}]	1217.06 ± 222.36
e	0.71 ± 0.22
ω [deg]	94.1 ± 64.0
γ [m s^{-1}]	-1099.5 ± 273.0
$m \sin i$ [M_{\odot}]	0.4 ± 0.1
semi-major axis [AU]	109 ± 7
offset _{Lick,setup13} [m s^{-1}]	0.0
offset _{Lick,setup6} [m s^{-1}]	-23.17
offset _{Lick,setup8} [m s^{-1}]	19.03
offset _{HARPS-N} [m s^{-1}]	-16294.87
independent long term trends	
RV slope _{Lick,setup2} [$\text{m s}^{-1} \text{ y}^{-1}$]	2.7 ± 5.5
RV slope _{Lick,setup13} [$\text{m s}^{-1} \text{ y}^{-1}$]	-13.8 ± 5.6
RV slope _{Lick,setup6} [$\text{m s}^{-1} \text{ y}^{-1}$]	-8.8 ± 3.4
RV slope _{Lick,setup8} [$\text{m s}^{-1} \text{ y}^{-1}$]	-18.6 ± 2.4
RV slope _{HARPS-N} [$\text{m s}^{-1} \text{ y}^{-1}$]	-36.6 ± 4.0

span (Fig. 7), which supports their stellar activity nature (discussed below in Sect. 6).

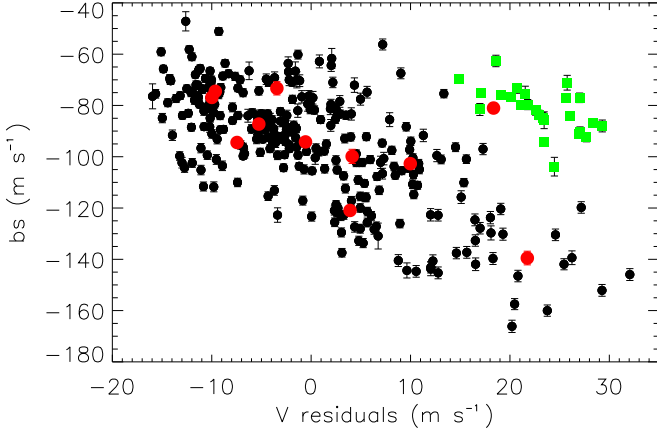


Figure 7. Residuals of the planetary fit for the HARPS-N measurements vs the pipeline-estimated bisector span. The green squares refer to exposures taken at JD 2456421, during which the target was observed between clouds. Red circles are the measurements for the nightly mean spectra. Error bars for the bisector span are taken as twice the RV error.

5.1. Stellar companion

Many astrometric measurements have been made to estimate the orbital parameters of the binary stellar system, with the most recent solutions (Roberts et al. 2011; Drummond 2014) claiming that the binary companion has a period < 1000 years and will approach periastron within the next two decades.

To check whether the RV data match the astrometric best-fit orbit well, we treated each Lick instrumental setup and HARPS-N separately. We fitted a one-planet model, imposing that the orbital solution for τ Boo b be fixed, and keeping a long-term linear trend free (lower part of Table 5). In this way, we were able to show the change of the slope in RVs caused by the binary companion τ Boo B for the first time. The information of the astrometric orbital parameters (Drummond 2014) and parallax (van Leeuwen 2007) indicates a mass sum of $1.8M_{\odot}$ and thus a value of $0.4M_{\odot}$ for τ Boo B. We used this value to calculate the astrometric-based orbital RV slope caused in τ Boo A by the stellar companion (Fig. 8).

Clearly, the data are insufficient for more constraints, but the best-fit astrometric solution agrees well with the present RVs. The fact that the slope calculated based on HARPS-N data is more than twice those calculated based on Lick data demonstrates that the star is rapidly accelerating as a result of the approaching periastron. A monitoring of the RV trend during the next years will enable us to obtain more reliable orbital parameters for the stellar binary companion.

6. Stellar activity

In this section we aim to study the SPMI in the τ Boo system. To this purpose, we extensively analyze and compare all the magnetic activity indicators available, both computed directly from the spectra and extracted from the CCF (see Sect. 3).

6.1. Analysis of the IRD vs IRD relationships

6.1.1. Ca II H&K and H_{α}

Figure 3 shows that the cores of the Ca II H&K lines are affected by variability that is stronger than noise in the corresponding

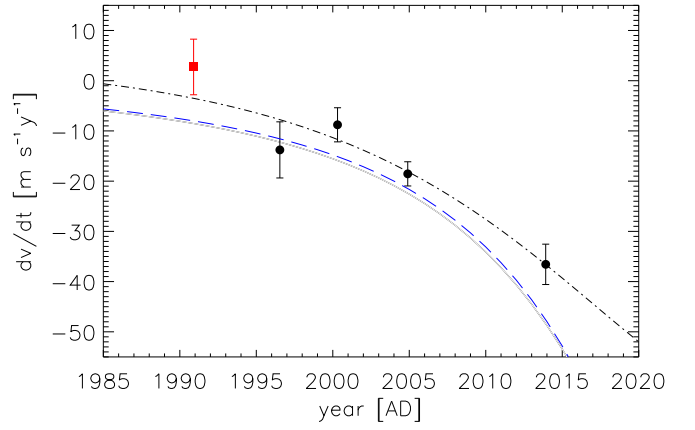


Figure 8. Points represent the values for the long-term RV slopes fitted on Lick and HARPS-N data. The red square is the value for the first Lick setup with large error bars, which was not taken in consideration when we fit the planetary parameters. The black dotted-dashed line represents the fitted orbit of the binary companion from the two-objects fit of Table 5. The blue dashed line is the long-term slope for the best-fit orbit for the stellar companion reported by Drummond (2014), assuming a mass value of $0.4 M_{\odot}$.

spectral regions. In Fig. 9 (left panel) we plot the corresponding IRDs of the two lines (IRD_H and IRD_K): we found that the two proxies are strongly correlated with each other with a confidence level of $\sim 94\%$; this shows that the detected signal is not an artifact produced by our data reduction, but arises from the magnetic activity of the star. The significance of the correlation was computed with 10000 random permutations of the data, which were also randomly perturbed by the corresponding uncertainties. Since the uncertainties on the variables are similar, the best-fit line was computed by means of a ranged major axis (RMA) regression (Legendre & Legendre 1983).

Since the two H and K proxies are strongly correlated, we averaged them to obtain the collective IRD_{HK} . We found that the latter strongly correlates with the canonical $\log R'_{HK}$ (Noyes et al. 1984) computed following Lovis et al. (2011) (Fig. 9, middle panel).

Moreover, as shown in Fig. 9 (right panel), IRD_{HK} also strongly correlates with $IRD_{H_{\alpha}}$. A similar result was obtained by Fares et al. (2009), who spectroscopically monitored the activity level of τ Boo in 2008. This is consistent with different studies by other authors (Meunier & Delfosse 2009; Martínez-Arnáiz et al. 2010, 2011; Stelzer et al. 2013; Gomes da Silva et al. 2014), who found strong pairwise correlations between the H&K and the H_{α} lines despite the different formation heights (lower and upper chromosphere) and adopting different approaches (e.g., single-epoch comparison of many stars, multi-epoch variability study of single objects, or emission line fluxes vs indices as relative measures).

6.1.2. Na I D_{1,2} doublet and He I D₃ triplet

We found that the IRDs of the Na I D₁ and Na I D₂ lines correlate linearly, but with a confidence level not better than $\sim 92\%$ (Fig. 10, left panel). We carefully checked the spectra and did not find any hint of a poor telluric correction or uncorrected terrestrial emission lines above the noise level. As described above for the H&K lines, we averaged the two proxies to obtain the IRD_{D12} indicator.

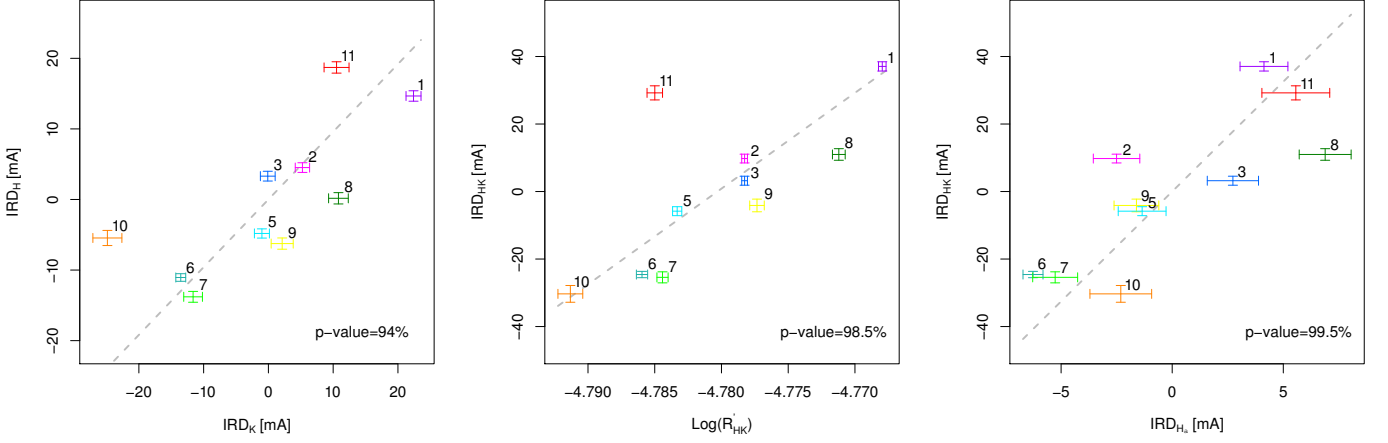


Figure 9. *Left panel:* IRD_H vs IRD_K . *Middle panel:* IRD_{HK} vs $\text{Log}(R'_{HK})$. *Right panel:* IRD_{HK} vs $IRD_{H\alpha}$. In all panels, the color code (online version only) is the same as in Fig. 3, while the number at the bottom is the confidence returned by the correlation test. The numbers above the data points indicate the ordered sequence in the series of observations. Gray dashes show the RMA best-fit.

We did not find any correlation from plotting IRD_{D12} against IRD_{HK} (Fig. 10, middle panel). This is consistent with the results of Díaz et al. (2007), who only found a good correlation between the Na and Ca doublets for stars with Balmer lines in emission (not the case of τ Boo). In any case, it is interesting to note that there is a bifurcation in the sample of measurements (Fig. 10, middle panel).

In a similar way, the IRD_{D12} vs IRD_{D3} plot seems to cluster into two subgroups (Fig. 10, right panel). The origin of the two trends is still unclear. Landman (1981), analyzing a few quiescent prominences on the Sun, obtained a similar bifurcation by comparing the intensities of the He I D₃ triplet with the Na I D₁ and D₂ lines. He conjectured, with no clear demonstration, that since the He triplet is back-heated by coronal UV radiation, then the two branches reflect the association of prominences with nearby coronal activity of different levels. The author remarked that the origin of the two branches is related to the He I D₃ triplet, as it shows the same bifurcation when compared to the intensity of the Ca II λ 8498 line, while the latter well correlates with the Na I D₁₂ lines. In contrast, we found the bifurcation when IRD_{D12} was compared with both IRD_{D3} and IRD_{HK} , while there is no bifurcation in the IRD_{D3} vs IRD_{HK} plot. Thus our results indicate that the formation of the Na I doublet should be investigated to explain this twofold behavior.

Another possibility is the presence of prominence-like structures around the stars, formed with matter evaporating from the planet and supported by the magnetic field of the star (Lanza 2014). Since exoplanets are expected to be richer in metal than stars (e.g., Fortney et al. 2006), this may explain why Na I shows the two branches instead of the He I D₃ triplet.

Focusing on the He I D₃ triplet, we found that the scatter of the IRD_{D3} measurements is slightly larger than the uncertainties, indicating that weak variability in this proxy has occurred, if any. Moreover, we did not find the correlation with the Ca II H&K lines that has previously been found by Garcia-Lopez et al. (1993) in their sample of F-type main-sequence stars. This is probably because their statistical sample spans a wide range of $\log R'_{HK}$, while τ Boo's chromospheric variability remained too limited during our observational campaign to detect such a correlation.

6.1.3. Parameters of the CCF

The very high S/N of the mean spectra allowed us to study the CCF variability with a high degree of accuracy. In particular, since the CCF is obtained from a large set of photospheric lines, the CCF variability is indicative of the source and level of photospheric activity. It is thus interesting to study the CCF profile to understand the phenomenology of magnetism on the surface of τ Boo and how it is related to chromospheric activity.

As suggested by Nardetto et al. (2006), one way to analyze the CCF profile is to retrieve its width and contrast to the continuum by means of a Gaussian best-fit. They also introduced the possibility to fit asymmetric profiles by tweaking the Gaussian model. For τ Boo, both methods led to poor fits of the observed CCF profiles, probably because the differential rotation combined with the rotation rate of the star broadens the line profile in a non-Gaussian way.

We therefore approached the CCF profile analysis by averaging the CCFs returned by the DRS from the series of ten nightly averaged spectra, obtaining a master CCF profile with a S/N higher than each nightly averaged CCF's S/N. Then, we fitted each nightly averaged CCF with the master CCF, allowing for changes in FWHM and contrast (CCFc).

We also computed the BIS and the v_{asy} parameters defined by Figueira et al. (2013). The former measures the velocity difference between the midpoints at the top and bottom of the CCF (Gray 2008), while the latter gives an estimate of the asymmetry of the CCF profile. By definition, the computation of both parameters is model independent.

Since Queloz et al. (2001), variations in BIS are the paradigm for the signature of activity-induced RV variations. These authors found a strong anticorrelation between the measured RVs and the corresponding BIS of the CCF. Since then, the anticorrelation between BIS and residual radial velocities (RV_{res} , the RVs minus the planetary best-fit orbit) is considered a clear signature of short-term (i.e., rotationally induced) photospheric variability. In our case, the BIS shows a high degree of anticorrelation with the residuals RV_{res} (Fig. 7). This suggests that RV_{res} are due to stellar activity.

Some other parameters show a strong anticorrelation: CCFc and FWHM (Fig. 11, left panel). This is consistent with the fact that while the FWHM measures the width of the CCF at half maximum, CCFc counteracts this to preserve the area of the

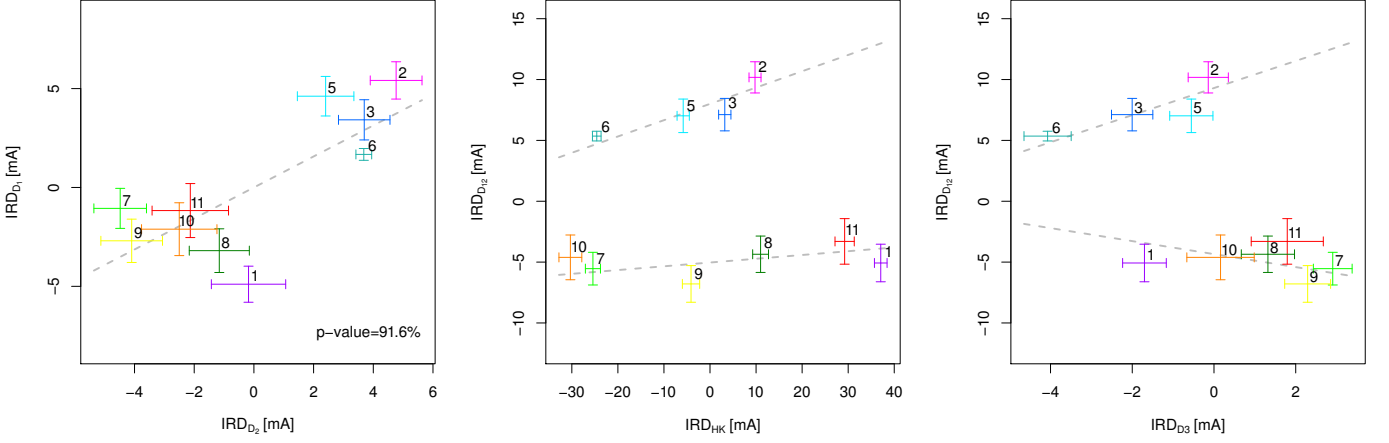


Figure 10. *Left panel:* IRD_{D1} vs IRD_{D2} . *Middle panel:* IRD_{D12} vs IRD_{HK} . *Right panel:* IRD_{D12} vs IRD_{D3} . In all panels, the color code (online version only) is the same as in Fig. 3 and represents different observation dates. The numbers above the data points indicate the ordered sequence in the series of observations. In the left panel, the number at the bottom is the confidence returned by the correlation test. In the middle and right panels, the two dashed gray lines are drawn by hand to highlight the bifurcation discussed in the text.

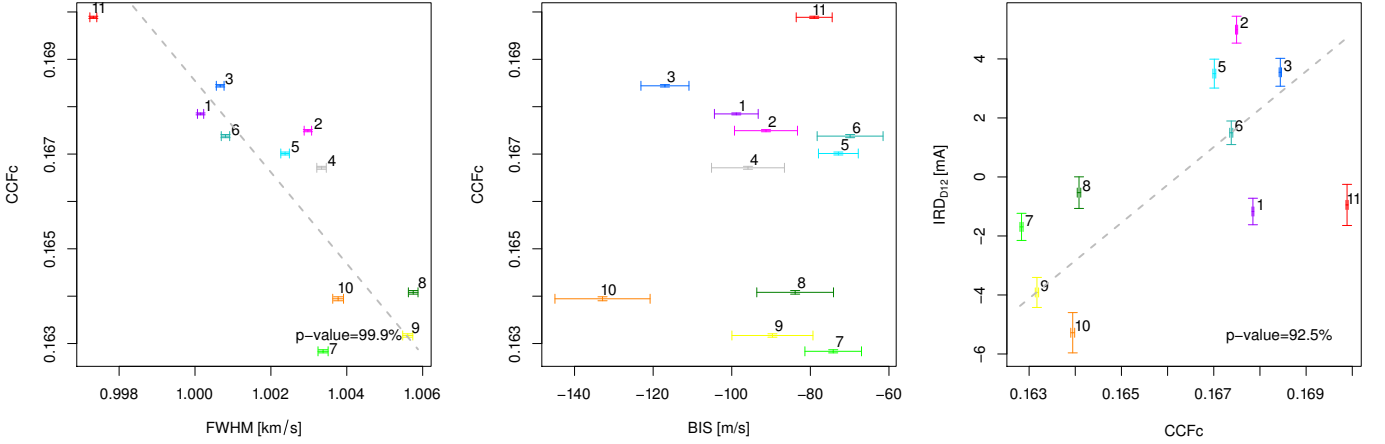


Figure 11. *Left panel:* $CCFc$ vs $FWHM$. *Middle panel:* $CCFc$ vs BIS . *Right panel:* IRD_{D12} vs $CCFc$. Symbols and colors (online version only) are the same as in Fig. 3.

CCF. The two indices are thus sensitive to the broadening of the wings of the CCF. We infer, accordingly, that correlations between these indices suggest a broadening variability of the CCF.

Our results therefore indicate that the BIS follows the deformations of the CCF better than $CCFc$ and $FWHM$ which, in turn, are sensitive to the overall width of the CCF. The BIS and $CCFc$ can then be considered the best representatives of two different families of indicators. Given the operational definitions of the BIS and $CCFc$, we regard the former as an indicator of the mean distortion of the line profile and the latter as an indicator of the mean strength of the photospheric lines.

The weak variability of BIS with respect to measurement uncertainties compared to $CCFc$ (Fig. 11, middle panel) may give some clues on the geometry of active regions on the stellar surface. The stability of the BIS and the variability of $CCFc$ may indicate that the CCF changes its contrast with respect to the continuum while preserving its overall asymmetry. This is consistent with a scenario with an active region around the pole of the star, which is not Doppler-shifted by stellar rotation and rapidly evolves in terms of contrast to the quiet photosphere (either in temperature difference and/or coverage factor).

We did not find any significant correlation between v_{asy} and the other parameters of the CCF.

When we compared the CCF parameters with the chromospheric indicators discussed in this section, we found the strongest correlation between IRD_{D12} and $CCFc$ ($p=92.5\%$, right panel in Fig. 11). The same applies for IRD_{HK} and $IRD_{H\alpha}$ with a lower confidence level ($p \leq 90\%$). We infer that the variability of the $Na I D_{12}$ doublet arises from changes in the line formation physics at the photospheric level, rather than from genuine chromospheric emission. The doublet is formed in the lower chromosphere (Tripicchio et al. 1997) and is thus more closely related to the magnetic activity of the lowest chromosphere and photosphere. Moreover, as stated above, the $Na I D_{12}$ doublet is a good proxy for chromospheric activity only for mid-to-late type stars with emission Balmer lines, which is not the case of τ Boo.

6.2. Time series analysis

Using the ephemeris of τ Boo b reported in Table 5, we searched for the eventual phasing of each of the indicators discussed so far with the orbital motion of the planet. The most convincing cases are the phase-folding of IRD_{HK} and $IRD_{H\alpha}$ shown in Fig. 12 (left and middle panel), where we set the phase $\phi = 0$ at the planetary inferior conjunction. In these diagrams we overplot the weighted least-squares best fit of the form $IRD = A \cdot \sin 2\pi\phi + B \cdot \cos 2\pi\phi + C$,

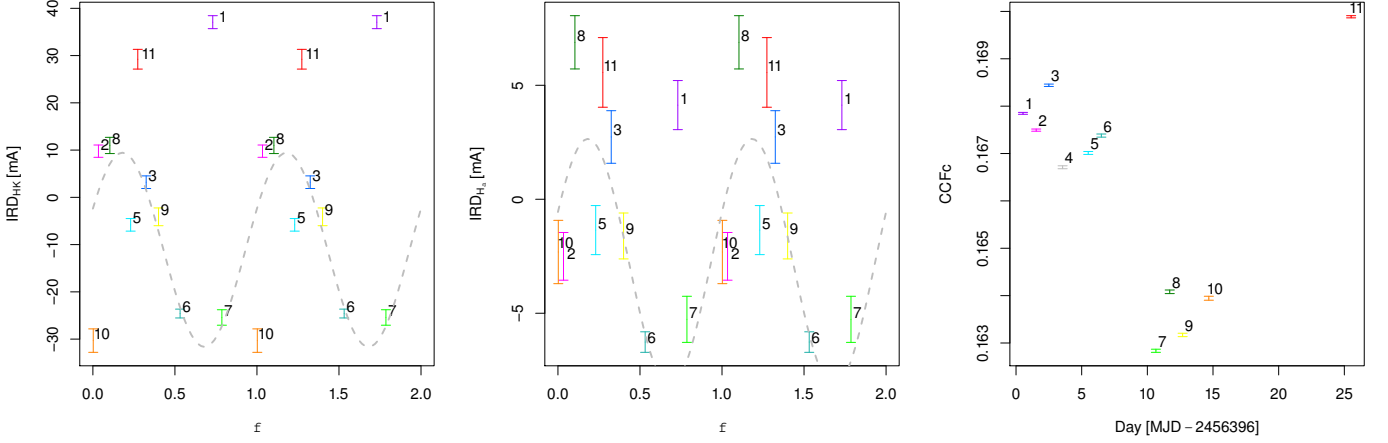


Figure 12. *Left panel:* Phase-folded diagram of IRD_{HK}. *Middle panel:* IRD_{H α} . *Right panel:* Time series of the CCFc measurements. The planetary inferior conjunction is at $\phi=0$. Colors (online version only) and numbers are the same as in the previous figures. In the left and middle panel, the gray dashed line is the least-squares best fit discussed in the text. We also report in the text the relative likelihood of the sinusoidal fit with respect to the flat model returned by the AICc.

where ϕ is the orbital phase and A, B, C are the parameters to be fitted. We excluded JD 2456396 (i.e., night 1) from the fit because it clearly is an outlier. The coefficient of determination R^2 of both fits is $\sim 50\%$, which means that the model explains $\sim 50\%$ of the total variance of the sample. Moreover, the likelihood ratio test suggests that the sinusoidal fit is to be preferred with respect to the flat model with a relative likelihood close to 100%.

For all the other indicators, both chromospheric and CCFc-related, we obtained a lower R^2 coefficient, that is, we found weaker or no evidence of such a phasing. Conversely, we found that CCFc, and consequently IRD_{D12}, show a clear trend with time (right panel in Fig. 12). If we interpret that CCFc anticorrelates with magnetic activity (either spot-like or plage-like, see Dumusque et al. 2014), then the decrease of CCFc between JD 2456402 and 2456407 suggests that τ Boo increased its activity level, and conversely it turned over toward a quieter configuration between JD 2456411 and 2456422.

6.3. Discussion

In Sect. 6.1 we argued that the CCFc shows variations on time scales longer than the stellar rotation. Polar magnetic regions on τ Boo have already been detected in several epochs by Fares et al. (2013), who remarked that the polarity of the magnetic field switches about every two years. Moreover, inside each activity cycle they found signatures of a rapid evolution of τ Boo’s magnetic field. This supports the hypothesis that the variations of CCFc are driven by a large-scale evolution of magnetic activity, even along time spans as short as ~ 20 days (Fig. 12, right panel).

Previous photometric monitorings of the star have never detected photometric variability above the mmag level (Baliunas et al. 1997; Walker et al. 2008). Accordingly, we assume that the typical peak-to-peak variability is on the order of 1 mmag (upper limit). With this assumption, and assuming that the active region is spot-dominated, we obtain that the active region covers $\sim 0.1\%$ of the visible hemisphere using the SOAP2.0 code (Dumusque et al. 2014). The corresponding peak-to-valley variations of RV, BIS, and FWHM returned by the simulations are $\lesssim 25$ m s $^{-1}$, while those of our measurements are actually larger (~ 50 m s $^{-1}$, ~ 70 m s $^{-1}$, and ~ 150 m s $^{-1}$ respectively).

Conversely, if we assume that the active region consists of a bright plage, then the coverage factor is $\approx 2.5\%$. With this coverage, the simulated activity-induced signal in RV, BIS, and FWHM is on the order of 100 m s $^{-1}$, comparable with those of our measurements. We thus conclude that the high-latitude active region probably is plage-dominated.

In Sect. 6.2 we briefly discussed the time variability of the most representative indicators, finding that the genuine chromospheric indicators, such as IRD_{HK} and IRD_{H α} , seem to be phased with the orbital motion of the planet. This has previously been found by Walker et al. (2008), who detected a plage on τ Boo at planetary phase $\phi \approx 0.8$ from Ca II H&K spectra in 2001 to 2003 and claimed a photospheric spot using MOST photometric data taken in 2004 and 2005. The authors stated that the persistence of the active region at the same longitude is a strong indication that it is caused by a magnetic link between the planet and the star. On the other hand, Mathur et al. (2014) have recently reported a few cases of bona fide single F-type stars observed with *Kepler* with active longitudes persisting on the stellar surface for many stellar rotations.

Since τ Boo’s rotational period equals the planetary period (with some degree of differential rotation, Fares et al. 2009), it is still unclear whether the phasing of chromospheric activity with the planet is due to SPMI or to an active region that simply corotates. In any case, if the SPMI scenario is confirmed, we remark that in our observing season the plage was located at $\phi \sim 0.1$ – 0.2 (Fig. 12), indicating that the magnetic connection between planet and star, if present, has moved between years 2005 and 2013. This may be due to a poloidal reversal of τ Boo’s magnetic fields between these epochs. However, we remark that at phase 0.8 we found the largest scatter in the activity diagnostics: we have only two observations, and no statistical significance of this hypothesis can be assessed.

7. Asteroseismology

We have shown in the previous sections how the mean spectra can be used to derive very precise radial velocity measurements to study the planetary and binary orbits and very accurate indicators to monitor the stellar activity and star-planet interaction. We now describe the results obtained from the analysis of the high-cadence, short-exposure HARPS-N spectra.

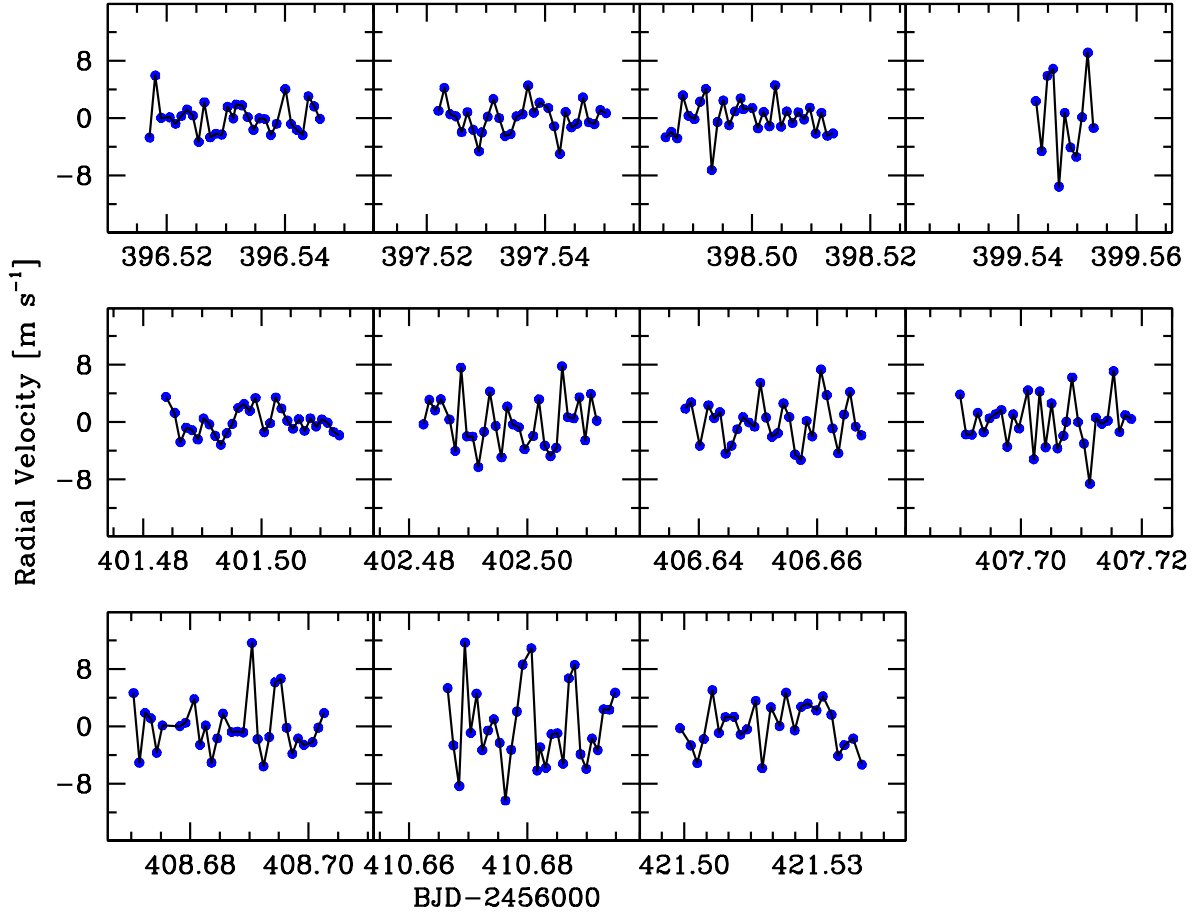


Figure 13. Asteroseismology of τ Boo: a linear fit was subtracted from the original HARPS-N data after the detrending from the planetary and binary orbits.

We started our asteroseismic analysis with correcting the Doppler shift that is due to the orbital motion of the planet (Sect. 5). Then, to remove the residual low-frequency term left in the data, several approaches were tried, and we report the most powerful approach here: the subtraction of a linear trend from the data of each night. This procedure ensured that no spurious low-frequency term (due to instrumental problems, planetary and binary orbits, or RV variations induced by activity phenomena with timescales longer than the duration of one observing sequence) affects the radial velocity measurements that were used for the asteroseismic analysis.

This procedure returned time series centered on $RV=0.0 \text{ m s}^{-1}$ on each night (Fig. 13). The resulting RV curves show sporadic peak-to-peak variations of up to 15 m s^{-1} (JD 2456399 and 2456410), but τ Boo typically is much quieter, at lower than 10 m s^{-1} . This amplitude is larger than that of the solar twin 18 Sco (Bazot et al. 2012), but comparable with that of the subgiant β Hyi (Bedding et al. 2007).

The time series were then analyzed in frequency to detect short-scale periodicities. We used the iterative sine-wave least-squares method (Vaniček 1971) and checked the results with the generalized Lomb-Scargle periodogram (Zechmeister & Kurster 2009). The power spectra are very similar and strongly affected by the sampling of the observations. The spectral window shows strong aliases at multiples of 1 d^{-1} , i.e., $11.57 \mu\text{Hz}$ (Fig. 14, inset in the top panel).

As expected because of the limited time coverage, the frequency analysis of the RV values cannot supply a unique determination of the asteroseismic content. The power spectrum is very noisy: a first relevant pattern occurs between 1.5 and 1.8 mHz, followed by another between 2.4 and 2.9 mHz (middle panel). Both are affected by the spectral window effects: each pulsational mode of τ Boo originates a structure similar to the spectral window, destroying the expected comb structure of the excited modes. The former pattern stands out a little more clearly over the noise, and it shows the highest peaks around 1.68 mHz (bottom panel). The corresponding period of 9.9 min can be glimpsed in Fig. 13: it is traced by six consecutive measurements (60 sec exposure time, 25-35 sec overhead), but of course often modified by the interference with the other modes. The amplitudes of the peaks are very small, around 1.1 m s^{-1} . This value takes into account the intrinsic incoherence (amplitude damping, mode lifetimes) of the solar-like oscillations. We also calculated the level of the noise in the RV time series and obtained 0.35 m s^{-1} . The corresponding $S/N=3.1$ leaves some uncertainties on the significance of the 1.5-1.8 mHz pattern since the threshold $S/N=4.0$ (e.g., Bedding et al. 2007) was not reached. All these observational uncertainties are due to the limited time coverage: twice as many measurements would have allowed us to reach a threshold of $S/N=4.0$.

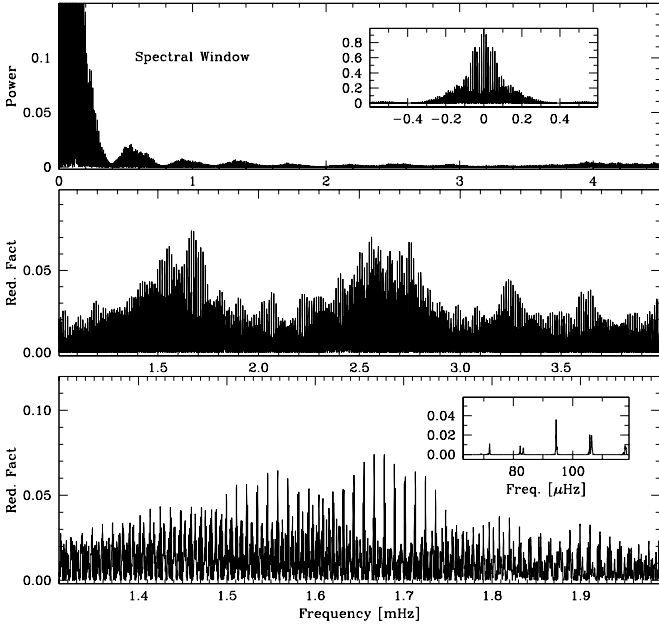


Figure 14. Asteroseismology of τ Boo. *Top panel:* spectral window of the HARPS-N data in the 0.0–4.5 mHz range and zoom in the 0.0–0.5 mHz range (inset). *Middle panel:* power spectrum in the 1.0–4.0 mHz range. *Bottom panel:* power spectrum in 1.3–2.0 mHz range and power spectrum of this spectrum (inset).

7.1. Asteroseismic results: observation vs theory

The availability of a small set of high-precision radial velocity measurements allowed us to obtain an estimate of the asteroseismic parameters of τ Boo making a very limited observational investment. We verify these results in a theoretical context.

We computed the expected place of an excess of power in a star like τ Boo. To do this, we used the scaling relations between stellar parameters (M , T_{eff} , and L ; Table 1) and the frequency of maximum power of the oscillations ν_{max} (e.g., Stello et al. 2009). We obtained 1.98 ± 0.46 mHz, compatible at $\pm 1\sigma$ level with the observed value. We performed another check on the detection of ν_{max} by computing the power spectrum of the power spectrum to identify regularities in the detected frequencies. The most relevant feature was the $11.57 \mu\text{Hz}$ spacing that is caused by the aliasing effect. After this, a peak at $94.4 \mu\text{Hz}$ has appeared (inset in the bottom panel of Fig. 14). If the structure centered at 1.68 mHz is due to solar-like oscillations, then the $94.4 \mu\text{Hz}$ spacing should be the large separation. The pair $(\nu_{\text{max}}, \Delta\nu) = (1680, 94) \mu\text{Hz}$ matches the observed relation (see Fig. 2 in Stello et al. 2009). Although not yet decisive, these results give us more confidence in the asteroseismic approach to study the stars hosting exoplanets by means of radial

velocity measurements performed mainly for other purposes.

8. Evolutionary stage

It has been well demonstrated (e.g., Cunha et al. 2007) that an accurate determination of mass and radius combined with the spectroscopic measurements of atmospheric parameters allows us to clearly constrain the stellar structure of observed stars.

To assess the information available from HARPS-N observations, we therefore calculated a grid of theoretical structure

models of τ Boo evolved from a chemically uniform model on the zero-age main sequence, using the ASTEC evolution code (Christensen-Dalsgaard 2008a) and varying the mass and the composition to match the available atmospheric parameters (see Table 4).

The evolutionary models have been produced by employing current physical information following the procedure described in Di Mauro et al. (2011). The input physics for the evolution calculations included the OPAL 2005 equation of state (Rogers & Nayfonov 2002), OPAL opacities (Iglesias & Rogers 1996), and the NACRE nuclear reaction rates (Angulo et al. 1999). Convection was treated according to the mixing-length formalism (MLT; Böhm-Vitense 1958) and defined through the parameter $\alpha = \ell/H_p$, where H_p is the pressure scale height. The initial heavy-element mass fraction Z_i was calculated from the iron abundance given in Table 4 using the relation $[\text{Fe}/\text{H}] = \log(Z/X) - \log(Z/X)_\odot$, where (Z/X) is the value at the stellar surface. We obtained $Z/X = 0.045 \pm 0.003$ assuming the solar value $(Z/X)_\odot = 0.0245$ (Grevesse & Noels 1993).

The resulting evolutionary tracks are characterized by the input stellar mass M , the initial chemical composition, and a mixing-length parameter.

The location of the star in the H-R diagram identifies τ Boo as being at the beginning of the main-sequence phase of core-hydrogen burning, with an internal content of hydrogen in the core of about $X_c = 0.5$. As predicted by Fares et al. (2009), it has a shallow convective region, with a depth of about $D_{\text{cz}} \approx 0.1R$, typical of stars in this phase. According to the stellar evolution constraints, given the match with the observed atmospheric properties, and with the use of all the possible values of mass and metallicity, our computations show that the age of τ Boo is 0.9 ± 0.5 Gyr and the mass is $M = 1.38 \pm 0.05 M_\odot$. It is clear that the accuracy on the values of age and mass here inferred are dependent on the stellar model calculation procedure, and in particular on the physical and chemical inputs (e.g., Lebreton et al. 2014). Here we simply note that lower values of the solar heavy-element abundance $(Z/X)_\odot$ led to a mass lower by 5% and an age higher by 30%. These values agree with those deduced above within $2\text{-}\sigma$ uncertainty limits. The lithium line at 6708\AA could not be used to confirm the young age, since $T_{\text{eff}} = 6399\text{K}$ (Table 4) puts τ Boo in the lithium dip (e.g., Balachandran 1995).

The value of age obtained by direct modeling is better constrained than the wide range of previous values obtained with different methods, such as the empirical relation between large-scale magnetic fluxes and age reported by Vidotto et al. (2014), chromospheric activity (Saffe et al. 2005; Henry et al. 2000), isochrone techniques (Saffe et al. 2005; Suchkov & Schultz 2001), or X-ray luminosity (Sanz-Forcada et al. 2010).

To reproduce the oscillations obtained in Sect. 7, we selected the models that best fit the observations among all the computed models. For the selected models we calculated the adiabatic oscillation frequencies using the ADIPLS code (Christensen-Dalsgaard 2008b). According to our calculations, this star should show solar-like pulsations with a spectrum in the interval $700 - 2600 \mu\text{Hz}$ and frequencies equally spaced by a large separation of about $\Delta\nu = 95 \pm 1 \mu\text{Hz}$. The observed large separation appears to agree excellently well with the theoretical separation. The range of frequencies is very similar, although the spectral window effects make a straight comparison very difficult. We conclude that there is no discrepancy between the values we inferred from the limited HARPS-N observations and the current modeling of solar-like oscillations in τ Boo.

8.1. Tidal evolution

Lanza (2010) and Damiani & Lanza (2015) found that the rotational period P_{rot} in a sample of main-sequence stars with $T_{\text{eff}} \gtrsim 6300$ K accompanied by hot Jupiters with orbital period P_{orb} verifies the relationship $1 \geq P_{\text{rot}}/P_{\text{orb}} \geq 2$ (cf. Fig. 10 in Damiani & Lanza 2015). Given its almost synchronous rotation, τ Boo satisfies this relationship as well. The timescale of tidal synchronization of the stellar rotation is at least 1 – 2 orders of magnitudes longer than the stellar age (e.g., Donati et al. 2008; Barker & Ogilvie 2009), suggesting that the system reached the ZAMS close to its current synchronous state. The subsequent evolution was characterized by a weak tidal interaction between the planet and the star with a very slow braking of the stellar rotation, owing to the low braking efficiency of the stellar winds of mid-F type stars (cf. Damiani & Lanza 2015, Sect. 6.1.2 for details). In other words, the present orbital and rotational angular momenta in the τ Boo system are probably close to the initial momenta with very little evolution since the system arrived on the ZAMS.

9. Conclusions

We studied the τ Boo system by means of a new observational strategy applied to HARPS-N spectra that were collected in the framework of the GAPS project. This strategy allowed us to obtain both high-cadence one-minute exposures to monitor the solar-like oscillations, and high S/N unsaturated spectra to study stellar activity and star-planet interaction.

We developed new computational tools to perform the co-addition of consecutive spectra and the subsequent average of them, preserving the correct computation of the BERV (and thus RV) values that have to be referred to the flux-balanced reference time. Implementing a custom mask for τ Boo allowed us to extract more accurate RV values; the adaptation of the Yabi platform gave us the possibility to test and verify these new tools in a user-friendly system.

Our results are summarized in the following points.

- We updated the ephemeris for the planet τ Boo b and showed by means of our RVs that the binary companion τ Boo B is rapidly accelerating, confirming the astrometric predictions that it is approaching the periastron on a highly eccentric orbit. We plan to take additional observations in the next years to have a more reliable value of its eccentricity.
- The SME software was applied to determine new stellar parameters, giving the same results as the equivalent width method. In particular, we refined the values of τ Boo's mass and radius to $1.39 \pm 0.25 M_{\odot}$ and $1.42 \pm 0.08 R_{\odot}$. We established that the star shows strong differential rotation, which we determined by means of both the LSD mean line profile and the CCF. We stress that the CCF computed by the HARPS-N pipeline can therefore be reliably used as an indicator of differential rotation.
- The analysis of the correlations between several indices pointed out evident chromospheric activity. In particular, the activity indicators extracted from HARPS-N spectra suggest the presence of a plage around one of the poles of the star. The nature of the chromospheric activity remains uncertain. It is unclear if it is due to SPMI or to a corotating active region, or both.
- Solar-like oscillations are detected in the RV time series. Although very limited by the spectral window, we inferred observational values of v_{max} and Δv . These values agree well

both with the scaling relations and the asteroseismic model computed from our stellar parameters. This result supports our confidence in the application of the asteroseismic approach to other bright stars hosting exoplanets to constrain their ages and masses.

- From the evolutionary point of view, τ Boo is at the beginning of the main-sequence phase of core-hydrogen burning, with an age of 0.9 ± 0.5 Gyr. The model we built allowed us to further constrain the value of the stellar mass to $1.38 \pm 0.05 M_{\odot}$ and thus, using $i = 44.5 \pm 1.5^{\circ}$ (Brogi et al. 2012), the mass of the planet to $6.13 \pm 0.17 M_{\text{Jup}}$.

Acknowledgements. The GAPS project acknowledges support from INAF through the "Progetti Premiali" funding scheme of the Italian Ministry of Education, University, and Research. We thank the referee G. Walker for interesting and useful comments that helped improve the clarity of the paper.

References

- Angulo, C., Arnould, M., Rayet M., et al. 1999, Nucl. Phys. A, 656, 3
 Balachandran, S. 1995, ApJ, 446, 203
 Baliunas, S. L., Henry, G. W., Donahue, R. A., et al. 1997, ApJ, 474, L119
 Barker, A. J., & Ogilvie, G. I. 2009, MNRAS, 395, 2268
 Bazot, M., Ireland, M. J., Huber, D., et al. 2012, A&A,
 Bedding, T. R., Kjeldsen, H., Arentoft, T., et al. 2007, ApJ, 663, 1315
 Biazzo, K., D'Orazi, V., Desidera, S., et al. 2012, MNRAS, 427, 2905
 Böhm-Vitense, E., 1958, Zeitschrift für Astrophysik, 46, 1115
 Borsa, F., Rainer, M., Poretti, E. 2013, Internal report GAPS-SCI-REP-006
 Brogi, M., Snellen, I. A. G., de Kok, R. J., et al. 2012, Nature, 486, 502
 Butler, R. P., Marcy, G. W., Williams, E., et al. 1997, ApJ, 474, L115
 Butler, R. P., Wright, J. T., Marcy, G. W., et al. 2006, ApJ, 646, 505
 Castelli, F., & Kurucz, R. L. 2004, arXiv:astro-ph/0405087
 Catala, C., Donati, J.-F., Shkolnik, E., et al. 2007, MNRAS, 374, L42
 Christensen-Dalsgaard, J. 2008a, Ap&SS, 316, 13
 Christensen-Dalsgaard, J. 2008b, Ap&SS, 316, 113
 Collier Cameron, A., Horne, K., Penny, A., & James, D. 1999, Nature, 402, 751
 Cosentino, R., Lovis, C., Pepe, F., et al. 2012, Proc. SPIE, 8446,
 Covino, E., Esposito, M., Barbieri, M., et al. 2013, A&A, 554, A28
 Cunha, M. S., Aerts C., Christensen-Dalsgaard J. et al. A&ARv 14, 217
 Damiani, C., & Lanza, A. F., 2015, A&A, 574, A39
 Di Mauro, M. P., Cardini, D., Catanzaro, G. et al., 2011, MNRAS, 415, 3783
 Diaz, R. F., Cincunegui, C., & Mauas, P. J. D. 2007, MNRAS, 378, 1007
 Donati, J.-F., Moutou, C., Farès, R., et al. 2008, MNRAS, 385, 1179
 Donati, J.-F., Semel, M., Carter, B. D., et al. 1997, MNRAS, 291, 658
 Drummond, J. D. 2014, AJ, 147, 65
 Dumusque, X., Boisse, I., & Santos, N. C. 2014, ApJ, 796, 132
 Fares, R., Donati, J.-F., Moutou, C., et al. 2009, MNRAS, 398, 1383
 Fares, R., Moutou, C., Donati, J.-F., et al. 2013, MNRAS, 435, 1451
 Figueira, P., Santos, N. C., Pepe, F., et al. 2013, A&A, 557, AA93
 Fischer, D. A., Marcy, G. W., & Spronck, J. F. P. 2014, ApJS, 210, 5
 Flower, P. J. 1996, ApJ, 469, 355
 Fortney, J. J., Saumon, D., Marley, M. S., et al. 2006, ApJ, 642, 495
 Garcia-Lopez, R. J., Rebolo, R., Beckman, J. E., & McKeith, C. D. 1993, A&A, 273, 482
 Gomes da Silva, J., Santos, N. C., Boisse, I., et al. 2014, A&A, 566, AA66
 Gratton, R. 2013, Internal report GAPS-SCI-REP-002
 Gray, D. F. 2008, The Observation and Analysis of Stellar Photospheres, by David F. Gray, Cambridge, UK: Cambridge University Press, 2008,
 Grevesse, N. & Noels, A. 1993 in Origin and Evolution of the Elements, ed. S. Kubono & T. Kajino, 14
 Henry, G. W., Baliunas, S. L., Donahue, R. A., et al. 2000, ApJ, 531, 415
 Hunter A.A., Macgregor A.B., Szabo T.O., et al., Yabi: An online research environment for Grid, High Performance and Cloud computing, Source Code for Biology and Medicine 2012, 7:1
 Iglesias, C. A., & Rogers F. J. 1996, ApJ, 464, 943
 Landman, D. A. 1981, ApJ, 251, 768
 Lanza, A. F. 2009, A&A, 505, 339
 Lanza, A. F. 2010, A&A, 512, AA77
 Lanza, A. F. 2012, A&A, 544, AA23
 Lanza, A. F. 2014, A&A, 572, LL6
 Lebreton, Y., Goupil, M. J., & Montalbán, J. 2014, EAS Publications Series, 65, 99
 Legendre, P., Legendre, L., 1998, Numerical Ecology, Elsevier
 Lockwood, A. C., Johnson, J. A., Bender, C. F., et al. 2014, ApJ, 783, L29
 Lovis, C., Dumusque, X., Santos, N. C., et al. 2011, arXiv:1107.5325

- Martínez-Arnáiz, R., Maldonado, J., Montes, D., et al. 2010, *A&A*, 520, AA79
- Martínez-Arnáiz, R., López-Santiago, J., Crespo-Chacón, I., & Montes, D. 2011, *MNRAS*, 414, 2629
- Mathur, S., García, R. A., Ballot, J., et al. 2014, *A&A*, 562, AA124
- Meunier, N., & Delfosse, X. 2009, *A&A*, 501, 1103
- Nardetto, N., Mourard, D., Kervella, P., et al. 2006, *A&A*, 453, 309
- Noyes, R. W., Hartmann, L. W., Baliunas, S. L., et al. 1984, *ApJ*, 279, 763
- Pepe, F., Mayor, M., Galland, F., et al. 2002, *A&A*, 388, 632
- Queloz, D., Henry, G. W., Sivan, J. P., et al. 2001, *A&A*, 379, 279
- Rainer, M. 2013, Internal report GAPS-SCI-REP-007
- Reiners, A., & Schmitt, J. H. M. M. 2002, *A&A*, 384, 155
- Reiners, A. 2003, *A&A*, 408, 707
- Reiners, A., Schmitt, J.H.M.M., 2003, *A&A*, 398, 647
- Reiners, A. 2006, *A&A*, 446, 267
- Roberts, L. C., Jr., Turner, N. H., ten Brummelaar, T. A., et al. 2011, *AJ*, 142, 175
- Rodler, F., Kürster, M., & Henning, T. 2010, *A&A*, 514, A23
- Rodler, F., Lopez-Morales, M., & Ribas, I. 2012, *ApJ*, 753, L25
- Rogers, F. J., Nayvonov, A. 2002, *ApJ*, 576, 1064
- Saffe, C., Gómez, M., & Chavero, C. 2005, *A&A*, 443, 609
- Santos, N.C., Israelian, G., Mayor, M., et al. 2004, *A&A*, 415, 1153
- Santos, N. C., Sousa, S. G., Mortier, A., et al. 2013, *A&A*, 556, AA150
- Sanz-Forcada, J., Ribas, I., Micela, G., et al. 2010, *A&A*, 511, LL8
- Scandariato, G., Maggio, A., Lanza, A. F., et al. 2013, *A&A*, 552, AA7
- Shkolnik, E., Walker, G. A. H., Bohlender, D. A., et al. 2005, *ApJ*, 622, 1075
- Shkolnik, E., Bohlender, D. A., Walker, G. A. H., & Collier Cameron, A. 2008, *ApJ*, 676, 628
- Sousa, S. G., Santos, N. C., Israelian, G., et al. 2007, *A&A*, 469, 783
- Stello, D., Chaplin, W.J., Basu, S., et al. 2009, *MNRAS*, 400, L80
- Stelzer, B., Frasca, A., Alcalá, J. M., et al. 2013, *A&A*, 558, AA141
- Suchkov, A. A., & Schultz, A. B. 2001, *ApJ*, 549, L237
- Tody, D. 1993, *Astronomical Data Analysis Software and Systems II*, 52, 173
- Torres, G. 2010, *AJ*, 140, 1158
- Tripicchio, A., Severino, G., Covino, E., et al. 1997, *A&A*, 327, 681
- Valenti, J.A., Piskunov, N.E. 1996, *A&A*, 118, 595
- van Leeuwen, F. 2007, *A&A*, 474, 653
- Vaniček, P. 1971, *Ap&SS*, 12, 10
- Vidotto, A.A., Gregory, S.G., Jardine, M. et al., 2014, *MNRAS*, 441, 2361
- Walker, G. A. H., Croll, B., Matthews, J. M., et al. 2008, *A&A*, 482, 691
- Wang, X., Sharon, Wright, J. T., Cochran, W., et al. 2012, *ApJ*, 761, 46
- Wright, J. T., & Howard, A. W. 2009, *ApJS*, 182, 205
- Zechmeister, M., & Kürster, M. 2009, *A&A*, 496, 577